Supplementary Materials

Observation of doubly-degenerate topological flatbands of edge states in strained graphene

Yongsheng Liang[1†], Jingyan Zhan[1†], Shiqi Xia[1*], Daohong Song[1, 2*], Zhigang Chen[1, 2*]

[1]*The MOE Key Laboratory of Weak-Light Nonlinear Photonics, TEDA Applied Physics Institute and School of Physics, Nankai University, Tianjin 300457, China*

[2]*Collaborative Innovation Center of Extreme Optics, Shanxi University, Taiyuan, Shanxi 030006, China*

[†]*These authors contributed equally to this work*

**Corresponding author: shiqixia@nankai.edu.cn, songdaohong@nankai.edu.cn, zgchen@nankai.edu.cn*

Section 1: Winding number under different boundary conditions in HCL

There are four fundamental boundaries (twig, zigzag, bearded, and armchair) in a honeycomb lattice (HCL), and the existence region of edge states in momentum space depends on the boundary condition. The winding loops predicting the existence of edge states for these boundaries in an unstrained HCL are displayed in Fig. S1(a). At the boundary of the corresponding one-dimensional Brillouin zone (1D BZ), the winding loop for the twig boundary forms a two-circle shape, while those for the zigzag and bearded boundaries form single circles. In contrast, the armchair boundary exhibits a straight-line. The nontrivial winding number ($w = 1$) for twig and zigzag boundaries indicates the presence of edge states at the boundary of the 1D BZ, whereas the trivial winding number ($w = 0$) for the bearded and armchair boundaries suggests that they cannot support edge states in the unstrained HCL at the boundary of the 1D BZ.

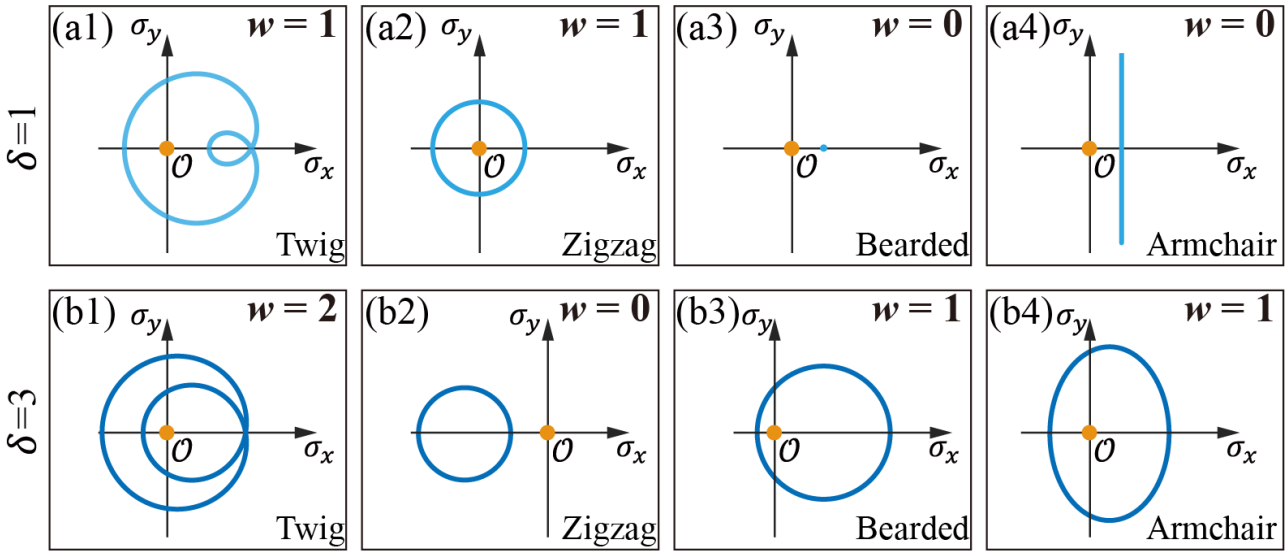

Fig. S1 Winding loop for different boundary conditions in HCL. (a) Winding loops in the (σ_x, σ_y) plane of unstained HCL corresponding to the twig boundary (a1), the zigzag boundary (a2), the bearder boundary (a3), and the armchair boundary (a4) at the boundary of the corresponding 1D BZ. The orange dot marks the origin point $\mathcal{O}$. (b) has the same layout as (a) but for the winding loop of a strained HCL under $\delta = 3$.

With the introduction of uniaxial strain, only the winding loop for the twig boundary achieves a winding number of 2, where the origin becomes encircled by the two circles (Fig. S1(b1)). For the other boundaries, the applied strain either shifts the circle, as seen for the zigzag (Fig. S1(b2)), enlarges the circle for the bearded boundary (Fig. S1(b3)), or transforms the straight line into a circle, as seen for the armchair boundary (Fig. S1(b4)). Therefore, the double degeneracy of flatbands can only be achieved in the HCL with a twig boundary condition.

Section 2: The relation between edge states and supercells in doubly degenerate flatbands.

In an HCL, if edge states form a flatband, the number of states within the flatband should match the number of sites along the boundaries. Here, we demonstrate the relationship between edge states and boundary sites in a strained HCL with twig boundaries. For an HCL ribbon with twig boundaries (Fig. S2(a)), there are $N_t = 10$ supercells (purple-shaded rectangles) and $2N_t = 20$ sites along the boundaries. After the gap opens due to uniaxial strain, 40 zero-energy modes are found to be localized at the twig boundaries (Fig. S2(b)), clearly indicating the formation of doubly degenerate flatbands. Furthermore, in momentum space, the vector $h(k)$ winds twice, covering the first, second, and

higher-order Brillouin zones (Fig. S2(c)), which further confirms the presence of doubly degenerate flatbands across the entire Brillouin zone.

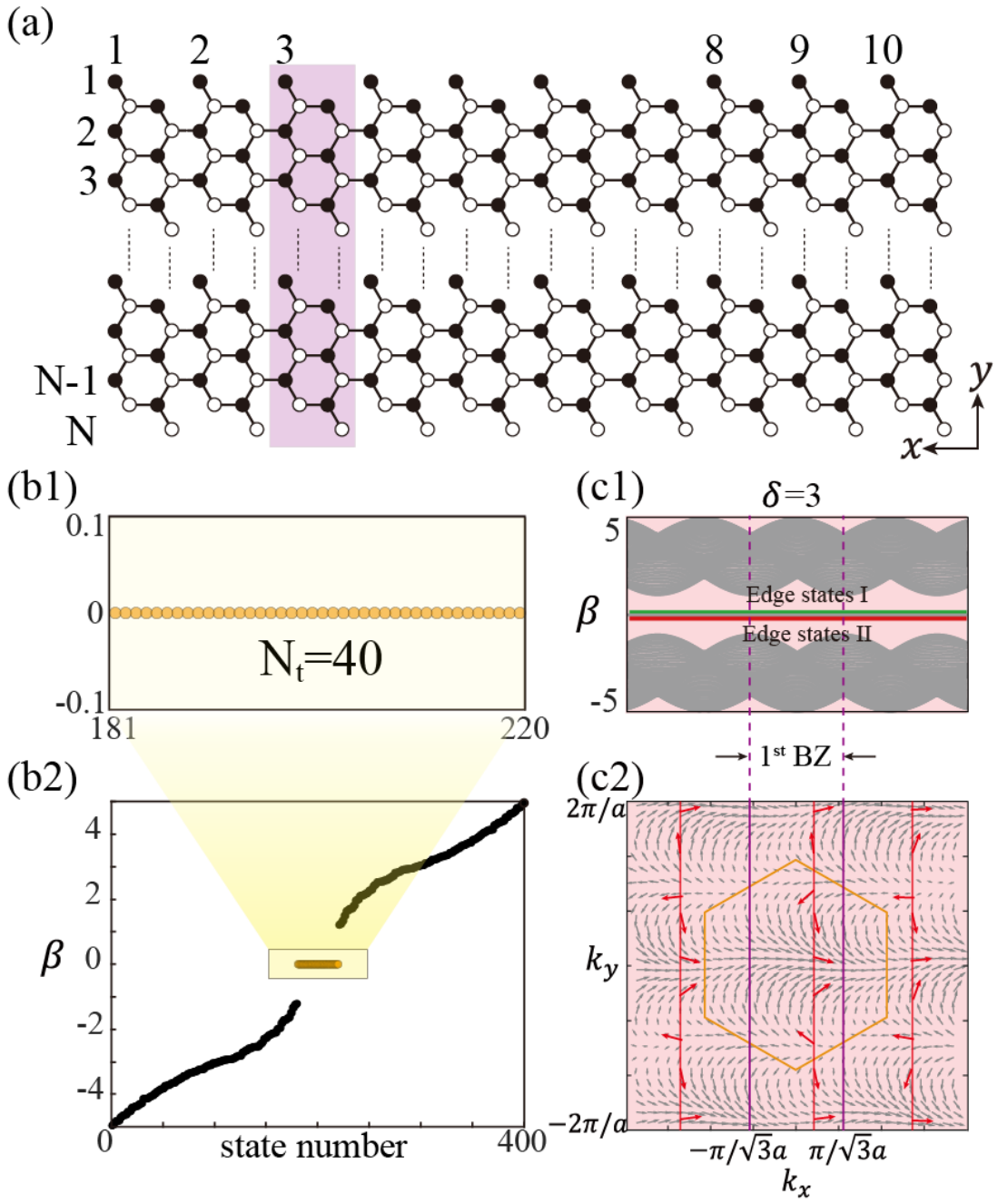

Fig. S2 Correlation Between Edge States and Boundary Sites in Strained graphene. (a) Schematic diagram of graphene ribbon with twig boundaries and periodic along the x-direction. The purple-shaded rectangle marks the supercell corresponding to the twig boundary and N marks the layers of the ribbon structure. (b1) The zoom-in zero-energy eigenvalue distribution in (b2). (b2) The energy spectrum for a finite-size strained graphene with twig boundary condition. (c1) The associated 1D band structure under $\delta = 3$. (c2) The corresponding schematics for the winding number calculation,

where the red arrows point in varying directions of the vector $\boldsymbol{h}(\mathbf{k})$. The winding number takes the value of $w = 2$ in the red shaded region, which determines the number of edge states.

Section3: Realization of four-fold degenerate flatbands in strained graphene.

In the main text, we demonstrate the realization of doubly degenerate topological flatbands by considering only the nearest-neighbor (NN) couplings. Here, we show the realization of multiple-fold (four-fold) degenerate flatbands by introducing long-range couplings. This is achieved by incorporating long-range A-B sublattice couplings (green curve in Fig. S3(a)) along with NN couplings $t_a = 1$ and $t_b = 3$. These couplings do not break the chiral symmetry, thereby preserving the flatness of flatband edge states. In this case, the off-diagonal component of the bulk Hamiltonian $h(\boldsymbol{k})$ takes the form:

$$h(\boldsymbol{k}) = t_a + t_b e^{i\boldsymbol{k}\mathbf{a_1}} + t_a e^{i\boldsymbol{k}\mathbf{a_2}} + t_c e^{2i\boldsymbol{k}a_2}$$

When $t_c > 3$, a four-fold degenerate flatband emerges at zero energy (red lines in Fig. S3(b)) for the system with a twig boundary. Meanwhile, the corresponding winding number $w = 4$ (Fig. S3(c)), fulfilling the "bulk-boundary correspondence".

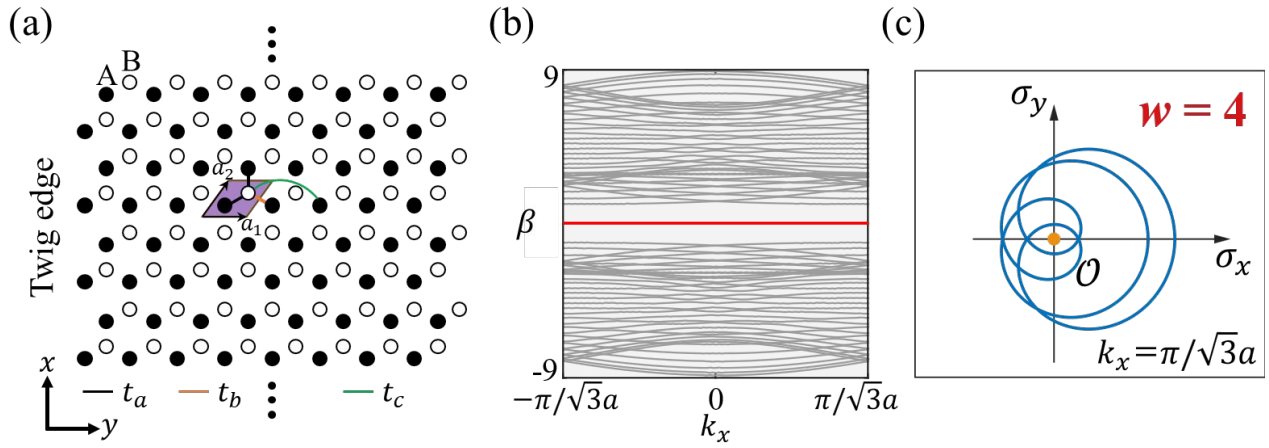

Fig. S3. Realization of four-fold degenerate flatbands. (a) Schematic diagram of the honeycomb lattice with twig boundaries and long-range couplings (t_c) indicated by green curve. The black and orange lines indicate the nearest-neighbor couplings (b) The corresponding 1D band structure of the strained honeycomb lattice with long-range coupling $t_c = 4$, where the red lines represent the region of edge states with four-fold degeneracy. (c) Winding loop for the twig boundary in the (σ_x, σ_y) plane at $k_x = \pi/\sqrt{3}a$. The orange dot marks the origin $\mathcal{O}$.

Section 4: Eigenmode distributions of doubly degenerate flatbands

For an unstrained HCL with a twig boundary condition, flatband edge states (edge states I) span the entire1D BZ. As discussed in the main text, tuning the coupling t_b while preserving chiral symmetry does not destroy edge states I but instead creates a new type of edge states (edge states II). The eigenmodes of edge states I under different coupling ratios and at different k_x are illustrated in Fig. S4(a). Edge states I persist at both the center and boundary of the 1D BZ before ($\delta = 1.5$) and after ($\delta = 3$) the gap opening. These states are localized at one sublattice and exhibit exponential decay into the bulk. In contrast, the existence region of edge states II is limited to the center of the 1D BZ before the gap opens ($\delta = 1.5$). The eigenmode of edge states II at $k_x = 0$ is shown in Fig. S4(b1). After the gap opens, edge states II span the entire BZ, forming a flatband. The corresponding eigenmodes at the center and boundary of the 1D BZ are shown in Fig. S4(b2, c2). Both edge states I and II exhibit exponential decay into the bulk but differ in their phase distributions: edge states I show opposite phases at the outermost A sublattices (marked as 1 and 3) of each supercell, while edge states II have identical phases.

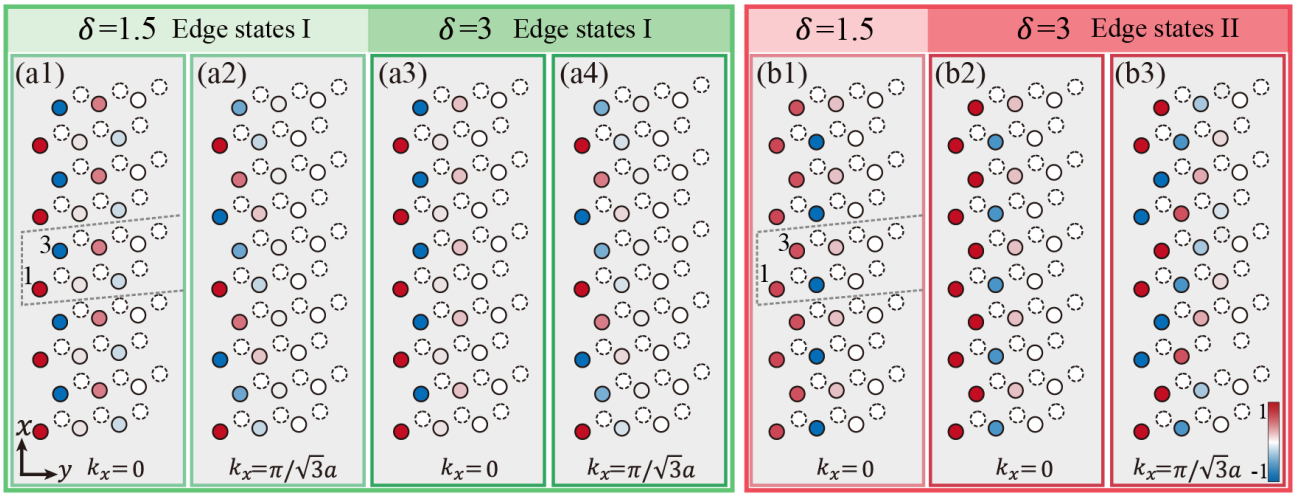

Fig. S4 Eigenmode distributions of twig edge states under different coupling ratios. (a) Eigenmode distribution of edge states I at $k_x = 0$ (a1) and $k_x = \pi/\sqrt{3}a$ (a2) under $\delta = 1.5$, and at $k_x = 0$ (a3) and $k_x = \pi/\sqrt{3}a$ (a4) under $\delta = 3$. Red and blue dots represent the opposite phase distributions. (b1, b2, b3) have the same layout as (a1, a3, a4) but show the eigenmode distribution of edge states II. The eigenmode of edge states II at $k_x = 0$ does not exist under $\delta = 1.5$.

Section 5: Experimental results of Edge states I in strained photonic graphene

As described in the main text, the topological flatband of edge states I is always present. Using continuous-wave (CW) laser-writing method and same experimental parameters, we fabricate HCLs with the desired boundary in a nonlinear crystal (SBN). The distances between nearest-neighbor sites are $d_1 = d_2 = 40.5\mu m$ and $d_3 = 34.5\mu m$ in the strained HCL corresponding to $\delta = 1.5$. The uniaxial strain direction is indicated by the gray arrow in Fig. S5(a). To demonstrate the existence of edge states I, probe beams matching the eigenmode distribution are generated using a spatial light modulator and sent into the strained HCL. The Fourier spectra of the input beams (insets of Fig. S5(b1, b2, c1, c2)) indicate that the probe beams targeting $k_x = 0$ and $k_x = \pi/\sqrt{3}a$ in momentum space are successfully achieved. The opposite phase distribution of the input beams at the outermost two A sublattices (marked as 1 and 3) showcases the mode feature for edge states I. The probe beams remain localized at both $k_x = 0$ and $k_x = \pi/\sqrt{3}a$ after 20 mm of propagation, with no light coupling into the B sublattices (indicated by the white arrows). For comparison, in-phase mixed bulk modes, where all the sites have the same phase distribution, are also considered. The corresponding outputs spread into the bulk under both $\delta = 1.5$ (Fig. S5(b3)) and $\delta = 3$ (Fig. S5(c3)). These results confirm that edge states I persist despite variations in the coupling ratio.

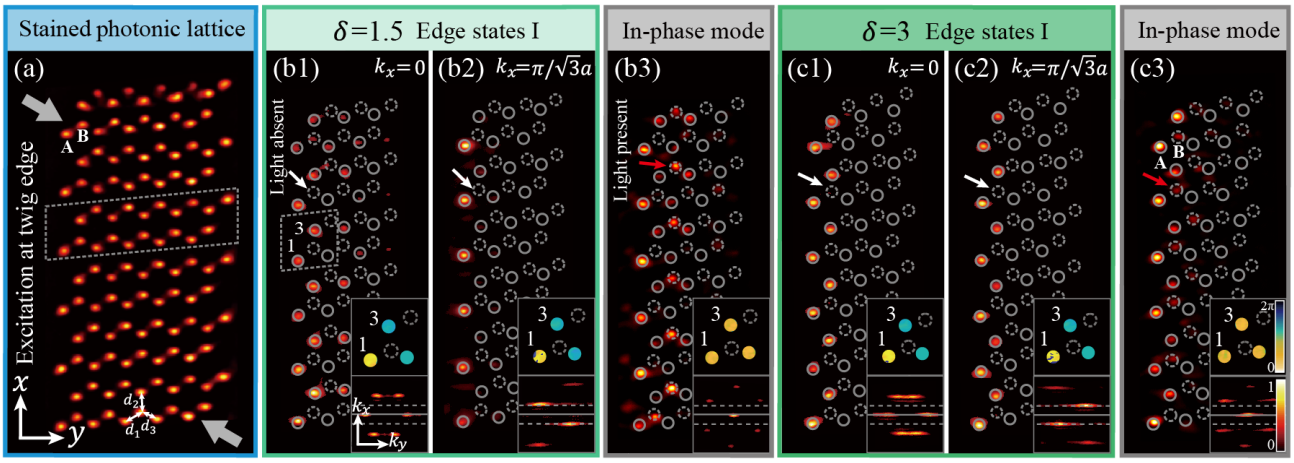

Fig. S5 Experimental observation of edge state I in strained photonic graphene. (a) A laser-written strained graphene lattice under twig boundary condition along the x-direction and the strain applied along d_3 direction at $\delta = 1.5$. The gray arrows indicate the uniaxial strain direction. A and B are two sublattices within the unit cell. (b) Experimental outputs of the probe beam matching the eigenmode of edge state I at $k_x = 0$ (b1) and $k_x = \pi/\sqrt{3}a$ (b2) under $\delta = 1.5$. (b3) Experimental

outputs of in-phase probe beam. The corresponding phase distributions within the dashed squares and Fourier spectra of the input beam are shown in the insets. The solid (dashed) lines in the Fourier spectra mark the center (edge) of the 1D BZ. (c) Results presented the same layout as (b) but they are for edge states I under $\delta = 3$. The red (white) arrows in (b) and (c) indicate the presence (absence) of light on the B sublattices. For all the experimental results, the propagation distance is $20\ mm$.

Section 6: Simulation results of twig edge states for a longer propagation distance

Due to the limited length of the crystal, we present simulation results of edge state propagation after 80 mm, using the same excitation conditions as in the experiment. The numerical results are obtained using the beam propagation method, in which the continuous Schrodinger equation is evolved in "time" (in propagation distance, z) in the HCL. The outputs are shown in Fig. S6. Since the structure cannot support a fully flatband for edge states II before the gap opens, the probe beam for edge states II at $k_x = \pi/\sqrt{3}a$ spreads into the bulk and occupies both A and B sublattice sites (Fig. S6(b2)). All other probe beams remain localized after 80 mm propagation (Fig. S6). These simulation results align with both experimental and theoretical findings, further confirming the double degeneracy of the flatband after the gap opens.

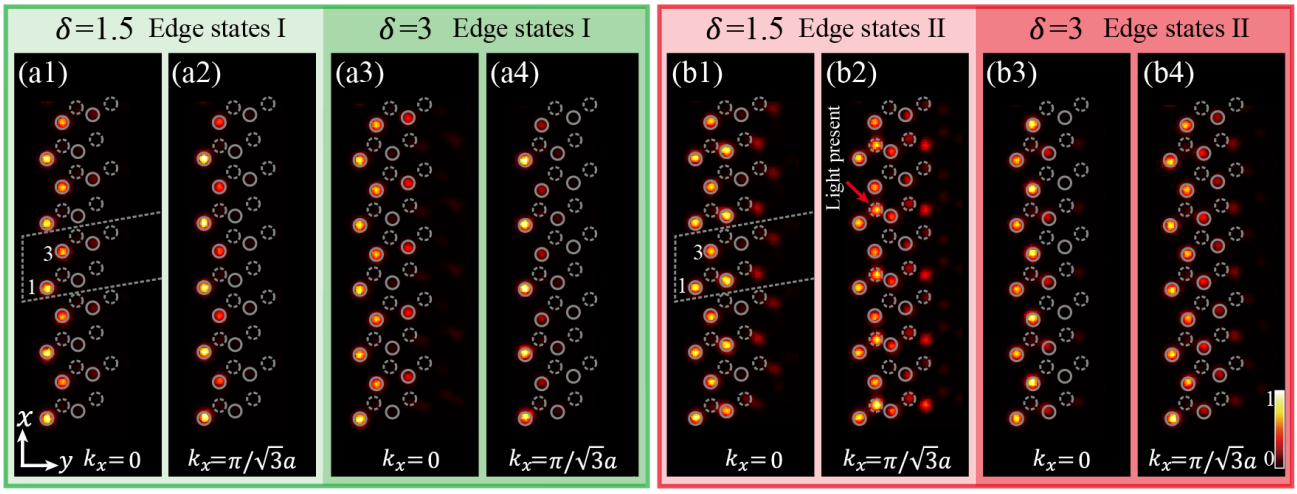

Fig. S6 Simulation results of twig edge states after 80 mm propagation. (a) Output of the probe beam matching the eigenmode of edge states I at $k_x = 0$ (a1) and $k_x = \pi/\sqrt{3}a$ (a2) under $\delta = 1.5$. (a3, a4) show the corresponding outputs of edge states I under $\delta = 3$. (b) has the same layout as (a), but shows the results of edge states II.

Section 7: Simulation results of compact edge states after longer propagation

Using the beam propagation method, we simulate the propagation of compact edge states (CESs). The input beam matching the eigenmodes of CES I and CES II are shown in Fig. S7(a1) and (b1). After 80 mm propagation, the probe beams remain intact, as illustrated in Fig. S7(a2) and (b2) for CES I and CES II, respectively. Due to the degeneracy of the flatbands, any linear combination of these two CESs can also remain compact and localized after propagation. As examples, we present the results for the combinations CES I + CES II and CES I − CES II. The intensity distributions of these combinations are shown in Fig. S7(c1) and (d1), respectively, with energy localized on the A sublattices and confined to a single supercell. After 80 mm propagation, the probe beams remain intact (Fig. S7(c2, d2)). The intensity distribution at the outermost sites can be precisely controlled by adjusting the overlap between CES I and CES II. For comparison, we simulate the propagation of in-phase modes, where the light spreads into the bulk after propagation (Fig. S7(a3-d3)). The realization of these hybrid compact edge states further confirms the degeneracy of two topological flatbands.

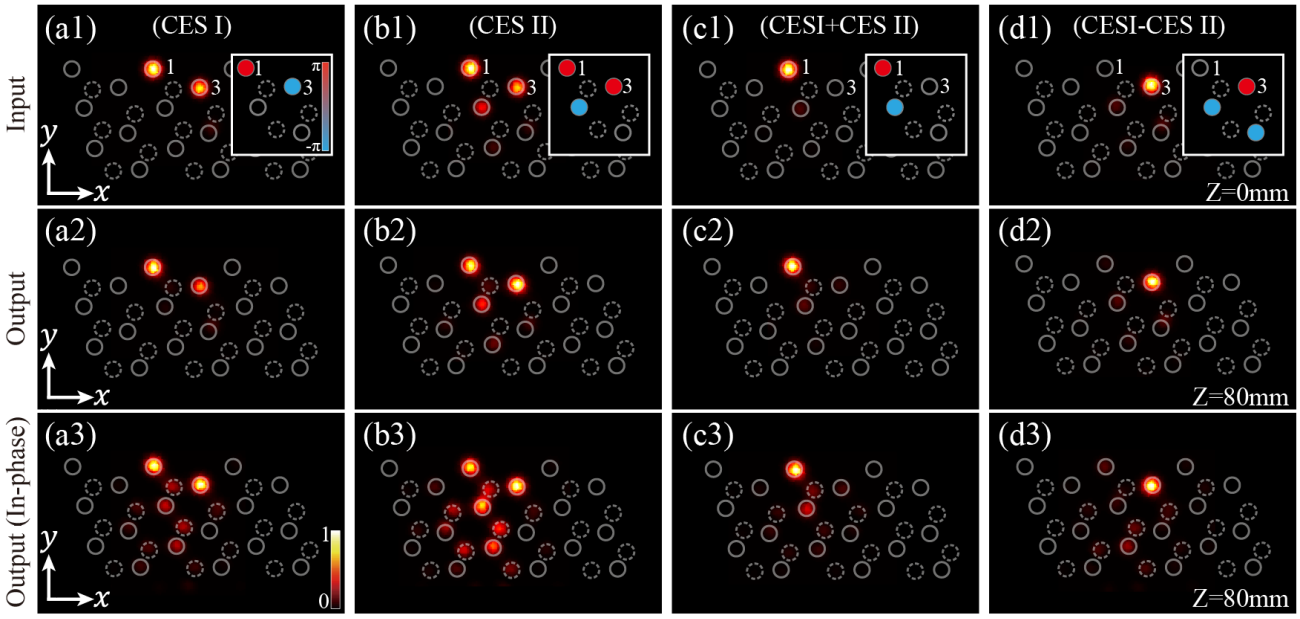

Fig. S7 Simulation results of compact edge states after 80mm propagation. (a1, b1) Intensity and phase (inset on the right) distributions of CES I and CES II at the input. (c1, d1) Intensity and phase distributions of the combinations CES I + CES II and CES I − CES II at the input. (a2-d2) The output of the probe beam (a1-d1) after $80\,mm$ of propagation, showing the CESs remain compact and localized. (a3-d3) Output of the in-phase beam as input for comparison.

Section 8: Simulation results of light confinement under different coupling ratios

We present the simulation results of light confinement at the twig edge in photonic graphene under different coupling ratios (δ) and excitation conditions. The input beam, with a Gaussian truncation along the boundary, excites only a subset of the boundary sites (Fig. S8(a). The excitation of edge states I or II is controlled by the phase matching between the input beam and the respective edge state. By varying momenta (k_x) of input beam with the mode distribution of edge states I, the light confinement ratio $\xi(k_x)$ for edge states I at different k_x is calculated under different coupling ratio δ (Fig. S8(b)). Here $\xi(k_x) = |\langle\phi_{k_x}|S|\phi_{k_x}\rangle|^2 / |\langle\phi_{k_x}|\phi_{k_x}\rangle|^2$, where ϕ_{k_x} represents the light distribution at the output facet under the excitation at k_x, and S is the projection operator on the four outer rows of the structure (marked by the green dashed rectangle in Fig. S8(a)). For $\delta = 1$, weak confinement near $k_x = 0$ arises due to the Dirac point, while strong confinement occurs away from $k_x = 0$, signifying the presence of edge states I. When the coupling ratio $\delta > 1$, edge states I span the entire 1D Brillouin zone, accompanied by an increase in $\xi(k_x)$. Similarly, the light confinement ratio of edge states II is calculated using the same method. For $\delta = 1$, the confinement ratio is relatively low, primarily contributed by the overlapping component from edge states I, indicating the absence of edge states II. At $\delta = 1.5$, edge states II form a mini-flatband in the red-shaded region, leading to a high $\xi(k_x)$ in this region. When $\delta = 3$, edge state II evolves into a complete flatband, yielding a high $\xi(k_x)$ across the entire 1D BZ. These simulation results align with theoretical predictions, further validating the evolution and existence of the edge states.

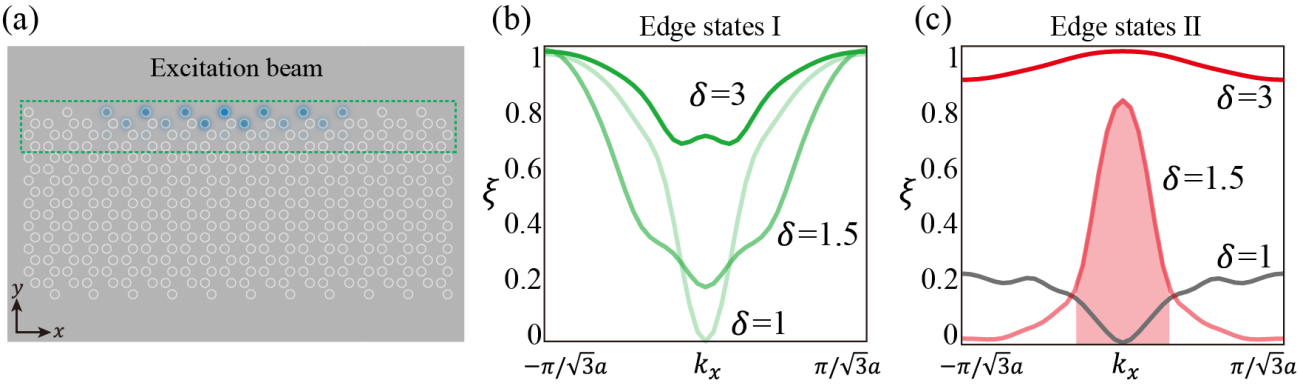

Fig. S8 The light confinement ratio under different coupling ratios. (a) Schematic of the intensity distribution of the input beam corresponding to edge state I or edge state II. (b) The light confinement ratio $\xi(k_x)$ for edge states I under different coupling ratios (δ). (c) same as (b), but for edge states II. The red-shaded region under $\delta = 1.5$ indicates the mini-flatband of edge states II.

Section 9: Perturbation analysis of topological flatband edge states

The presence of edge states I and edge states II are predicted by the nontrivial winding number. One of the most relevant properties of these edge states is their robustness against perturbations that preserve chiral symmetry. To investigate the robustness, we numerically apply chiral-symmetry-preserving perturbations to the nearest-neighbor couplings, i.e., $t'_{a(b)} = t_{a(b)} + \tau$, where $t_a = 1$, and $t_b = 1$, 1.5, and 3 correspond to different coupling ratios. The strength of the random perturbations is set to 0.5 ($\tau = 0.5 * ((rand(1) - 0.5) * 2)$. The results reveal that both edge state I (green line) and edge state II (red line) remain robust under different coupling ratios, with their energies pinned at zero, while the bulk modes are significantly affected (Fig. S9(a)). For the gapped case ($\delta = 3$), as the strength of random perturbations increases, the bulk modes are increasingly affected, whereas the edge modes remain stable and pinned at zero energy (Fig. S9(b)).

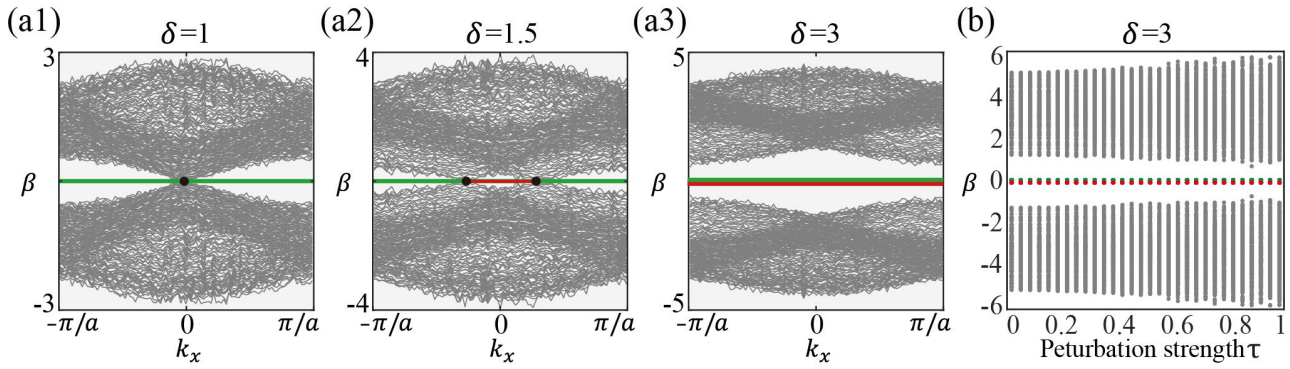

Fig. S9 Perturbation analysis of topological flatband edge states. (a) Robustness of topological flatbands in the HCL for coupling ratio $\delta = 1$ (a1), $\delta = 1.5$ (a2), $\delta = 3$ (a3), under perturbations ($\tau = 0.5$) applied to site couplings while preserving chiral symmetry. The green lines and red lines represent the existence regions of edge states I and edge states II, respectively. Black dots mark the degenerate points. (b) The eigenvalue distribution of gapped HCL ($\delta = 3$) under perturbations with increasing strengths τ.

Section 10: Experiment setup for photonic graphene fabrication with desired boundary condition

Experimentally, we fabricate the strained graphene lattice by using a cw-laser writing method. The core concept involves site-to-site writing of waveguide in a nonlinear crystal using a set of precisely modulated, non-diffracting writing beams, which are controlled by a spatial light modulator (SLM).

Due to the memory effect of the nonlinear crystal, the writing beams induce changes in the refractive index upon illumination, ultimately resulting in the formation of the designed photonic lattice structure. In this process, the writing Gaussian beam has a wavelength of 488 nm and an FWHM of 8 μm. The spacing between nearest-neighbor waveguides is modified by the SLM and adjusted based on the coupling ratio of the strained graphene lattice, allowing precise control over the coupling between the waveguides.

As shown in Fig. S10, we present the experimental setup for generating photonic graphene fabrication. Given that the non-diffracting zone of the Gaussian beam is too short to cover the crystal length, an approach similar to femtosecond laser direct writing technology is adopted in the experiment. The writing beam is generated via a SLM and a 4F system after correcting the aberration. Firstly, the position of writing beam is fixed, and the crystal is placed on a motorized translation stage which can move along the propagation direction of the Gaussian beam. Due to the memory effect, a single waveguide is formed in the crystal. By precisely controlling the position of the Gaussian beam in the transverse plane via the SLM, we realize site-to-site fabrication of strained graphene lattice with a twig boundary and exhibiting different coupling ratios.

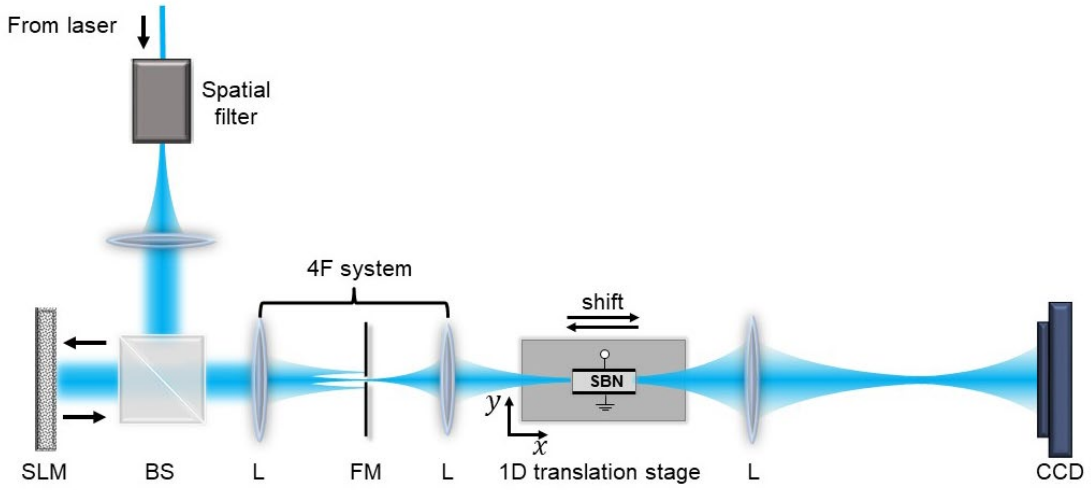

Fig. S10 Experimental setup for photonic graphene fabrication in a nonlinear crystal. SLM, spatial light modulator; BS, beam splitter; L, lens; FM, Fourier mask; SBN, strontium barium niobite. CCD, charge coupled device.

Section 11: Experimental method for the construction of the probe beams

To generate the probe beam of edge states, its intensity and phase distributions are matched to the eigenmodes of edge states at various k_x. An SLM is used to construct the probe beams, with grayscale values of each pixel representing phase changes from 0 to 2π, enabling precise phase modulation. Additionally, a grating phase mask is added to the SLM to adjust the first-order diffraction efficiency, allowing fine control over the beam intensity. Ultimately, the probe beams are meticulously designed to align with the eigenmodes of the different edge states.

For example, in the experiment, we construct probe beams that match the eigenmodes of two topological twig edge states at $k_x = 0$ and $k_x = \pi/\sqrt{3}a$. The constructed probe beams matching edge states I are shown in Fig. S11. The intensity and phase of probe beams at each site are independently modulated, with light is exclusively distributed on the A sublattice (Fig. S11(a1, b1, c1, d1)). The corresponding phase distributions are shown in Fig. S11(a2, b2, c2, d2). Similarly, all probe beams for edge states II are constructed and shown in Fig. S12 using the same method. The identical phase distribution at the outermost A sublattices (marked as 1 and 3) of each supercell distinguishes edge state II from edge state I (Fig. S12).

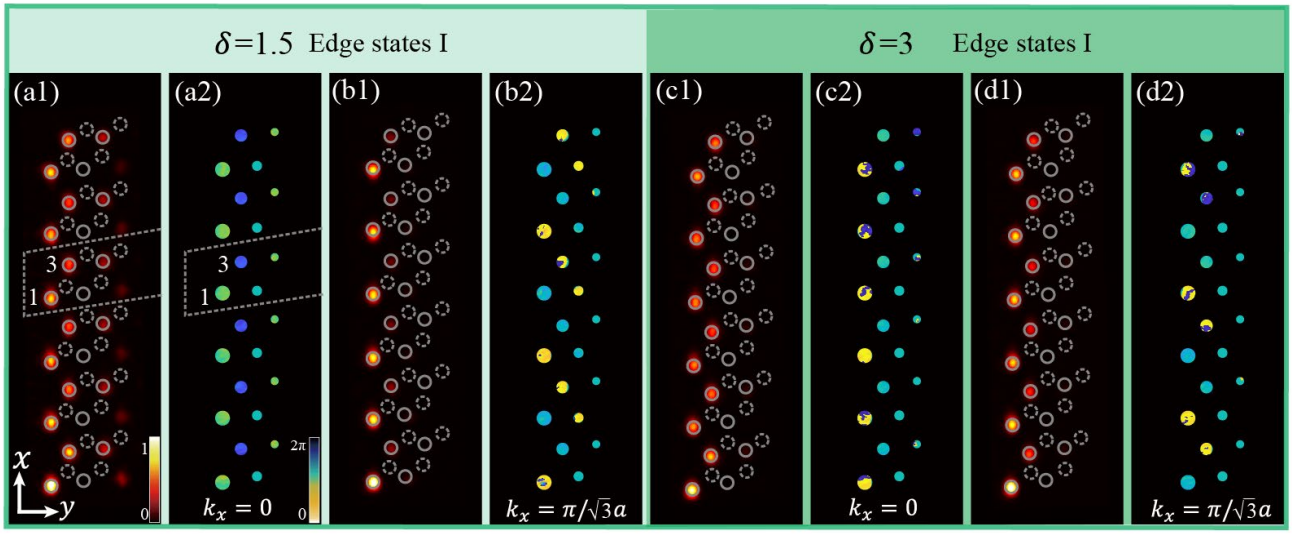

Fig. S11 Intensity and phase patterns of input probe beams for edge sates I. (a) Intensity distributions of probe beams matching the eigenmodes of edge states I at $k_x = 0$ (a1) and $k_x = \pi/\sqrt{3}a$ (b1) under $\delta = 1.5$, and at $k_x = 0$ (c1) and $k_x = \pi/\sqrt{3}a$ (d1) under $\delta = 3$. The energy is only distributed at A sublattices and exhibits exponentially decay into the bulk. (a2-d2) Phase distributions of probe beams corresponding to (a1-d1).

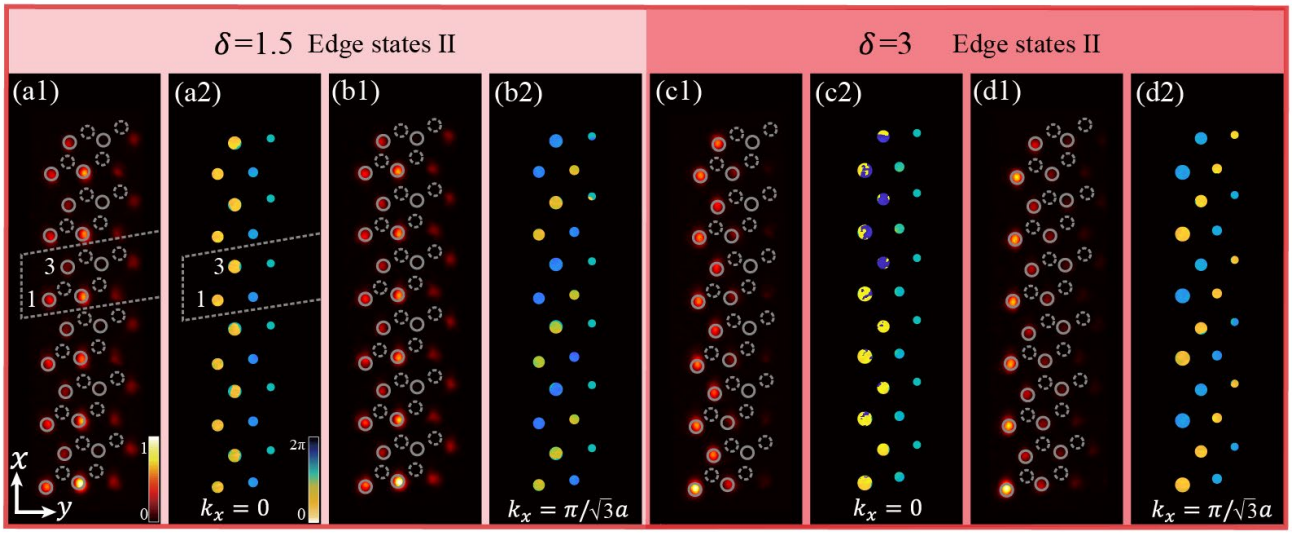

Fig. S12 Intensity and phase patterns of input probe beams for edge sates II. (a) Intensity distributions of probe beams matching the eigenmodes of edge states II at $k_x = 0$ (a1) and $k_x = \pi/\sqrt{3}a$ (b1) under $\delta = 1.5$, and at $k_x = 0$ (c1) and $k_x = \pi/\sqrt{3}a$ (d1) under $\delta = 3$. The energy is only distributed at A sublattices and exhibits exponentially decay into the bulk. (a2-d2) Phase distributions of probe beams corresponding to (a1-d1).